ARTICLE

Bionic Multi-Interface Evaporator for Omnidirectional Solar-Driven Reverse Multistage Desalination

Received 00th January 20xx,
Accepted 00th January 20xx

DOI: 10.1039/x0xx00000x

Wenzong Li [a,b], Lemin Zhang [a], Jiahui Chu [a], Xu Wang [a], Xiangge Bai [a], Shile Feng [a], Yahua Liu [a,b*]

Supplementary Note:

S1. Cost Analysis

The cost of a 0.5 mm-thick 5052 aluminum alloy sheet is approximately \$5 m^{-2}, and the nanosecond laser processing cost is about \$4.5 m^{-2}, yielding a total fabrication cost of ~ \$9.5 m^{-2}. In comparison, conventional polyurethane desalination membranes[1, 2] involve more complex fabrication processes and cost approximately \$27.7 m^{-2}.

Moreover, seawater desalination using semipermeable membranes requires complex electrical systems and consumes more than 2 kWh of electricity per cubic meter of freshwater produced[3]. In contrast, our system operates solely on solar energy, eliminating the need for external power input and offering a more sustainable long-term solution.

S2. Characterization of the photothermal coating

Figure S3a shows a scanning electron microscope image of the BC&Fe_3O_4 photothermal coating, which features densely packed, mountain-like microscale structures. Energy-dispersive spectroscopy analysis confirms that these microscale structures are composed primarily of Fe, C and O elements (Figure S3b).

S3. Flow path in the multistage evaporator

The RDE is mounted on an inclined support equipped with a diversion channel. The inclined support is positioned above a seawater reservoir system comprising a seawater reservoir and a brine collection tank. Seawater is delivered to the evaporation interface of each stage through absorbent paper, while the generated brine is guided to the brine tank via the same pathway. The freshwater produced at each stage is discharged through an outfall and subsequently collected (Fig. S9).

S4. Solar-to-steam conversion efficiency of RME under horizontal irradiation

The solar-to-steam conversion efficiency of a multistage evaporator under horizontal illumination can be expressed[4] as

$$\eta = q/C_{\mathrm{opt}}P_{\mathrm{o}} \tag{1}$$

where C_{opt} is the optical concentration, P_o is the solar irradiance (1 kW m^{-2}), and q is the vaporization heat flux defined as

$$q = h_{\mathrm{v}}m \tag{2}$$

Here, m is the evaporation rate, and h_v is the enthalpy of vaporization of water (2350 J g^{-1}). Under horizontal irradiation, the intermediate stages exhibit suppressed evaporation, limiting latent heat recovery from condensation. In contrast, the illuminated side sustains enhanced evaporation, where the latent heat released upon condensation is efficiently recycled to elevate the interfacial temperature of each intermediate evaporation layer (Fig. S11a). The maximum temperature rise reaches ~3 °C (Fig. S11b). Consequently, the system maintains a high evaporation rate of 4.55 kg m^{-2} h^{-1}, corresponding to a photothermal conversion efficiency of ~300%. This efficient recycling of latent heat results in an overall energy efficiency exceeding 100%.

S5. COMSOL simulation process and parameters

Solar radiation transport in the arched evaporator was investigated using a transient model developed in COMSOL Multiphysics® 6.2. Transient heat transfer within the evaporator is governed by the energy conservation equation

$$\rho C_{\mathrm{p}}\frac{\partial \mathrm{T}}{\partial \mathrm{t}} + \rho C_{\mathrm{p}}\mathbf{u}\cdot\nabla \mathrm{T} + \nabla\cdot q = Q + Q_{\mathrm{ted}} \tag{3}$$

where ρ is the material density, C_{p} is the specific heat capacity, T is the temperature, and t denotes time. The second term on the left-hand side represents convective heat transport induced by the fluid velocity field $\mathbf{u}$, while q is the conductive heat flux. According to Fourier's law, the conductive heat flux q is expressed as

$$q = -k\nabla \mathrm{T} \tag{4}$$

where k is the thermal conductivity. On the right-hand side of Eq. (1), Q denotes the volumetric heat source, and Q_{ted} accounts for additional heat generation or dissipation processes, such as evaporation–induced cooling or radiative heat exchange. The total radiative heat flux of the ith interface,

[a.] State Key Laboratory of High-performance Precision Manufacturing, Dalian University of Technology, Dalian 116024, P. R. China.
[b.] Department of Anaesthesiology, Central Hospital of Dalian University of Technology, Dalian 116033, China.

J_i, is given by the sum of its thermal emission and reflected incident radiation

$$J_i = \varepsilon_i e_{\mathrm{b}}(T)\mathrm{EFP}_i(T) + \rho_{\mathrm{d},\,i} G_i \quad (5)$$

where ε_i is the hemispherical emissivity of the interface, $e_{\mathrm{b}}(T)$ is the blackbody emissive power at temperature T, $FEP_i(T)$ represents the fraction of emitted power within the effective spectral band, $\rho_{\mathrm{d},\,i}$ is the diffuse reflectivity, and G_i is the total incident radiative irradiation on the *i*th interface. The total irradiation G_i consists of contributions from neighboring surfaces $G_{\mathrm{m},\,i}$, the ambient environment $G_{\mathrm{amb},\,i}$, and external sources $G_{\mathrm{ext},\,i}$

$$G_i = G_{\mathrm{m},i} + G_{\mathrm{amb},i} + G_{\mathrm{ext},i} \quad (6)$$

The ambient radiation term is calculated as

$$G_{\mathrm{amb},\,i} = F_{\mathrm{amb},\,i}\varepsilon_{\mathrm{amb}} e_{\mathrm{b}}(T_{\mathrm{amb}})FEP_i(T_{\mathrm{amb}}) \quad (7)$$

where $F_{\mathrm{amb},\,i}$ is the view factor between the ambient environment and the *i*th interface, $\varepsilon_{\mathrm{amb}}$ is the effective emissivity of the ambient medium, and T_{amb} is the ambient temperature. The blackbody emissive power $e_{\mathrm{b}}(T)$ follows the Stefan–Boltzmann law modified by the refractive index n as

$$e_{\mathrm{b}}(T) = n^2\sigma T^4 \quad (8)$$

where σ is the Stefan–Boltzmann constant. The fractional emitted power $FEP_i(T)$, accounting for the spectral distribution of thermal radiation over a wavelength range $[\lambda_{i-1}, \lambda_i]$, is derived from Planck's law as

$$\mathrm{FEP}_i(T) = \frac{15}{\pi^4}\int_{C_2/(\lambda_{i-1}T)}^{C_2/(\lambda_i T)} \frac{\mathrm{x}^3}{1 - \mathrm{e}^{\mathrm{x}}} d\mathrm{x} \quad (9)$$

where C_2 is the second radiation constant.

Boundary conditions

(1) The ambient temperature was set to T_{amb} = 293.15 K. Because only surface emissivity is considered, half-day temperature variations were neglected (dT=0).

(2) All boundaries were assumed to be thermally insulated except for the photothermal interface.

(3) The photothermal interface was prescribed as a heat-flux boundary condition.

Geometry

The arched evaporator was modeled in three dimensions (Figure S13), with a top evaporation interface area of approximately 600 mm² and a side evaporation interface area of approximately 755 mm².

References

1 Y. J. Yao, P. X. Zhang, F. Sun, W. Zhang, M. Li, G. Sha, L. Teng, X. Z. Wang, M. X. Huo, R. M. DuChanois, T. C. Cao, C. Boo, X. Zhang and M. Elimelech, Science, 2024, 384, 333-338.

2 G. Amy, N. Ghaffour, Z. Li, L. Francis, R. V. Linares, T. Missimer and S. Lattemann, Desalination, 2017, 401, 16-21.

3 Y. J. Lim, K. Goh, M. Kurihara and R. Wang, J. Membr. Sci., 2021, 629, 119292.

4 L. Zhang, Z. Xu, B. Bhatia, B. Li, L. Zhao and E. N. Wang, *Appl. Energy.* 2020, **266**, 114864.

Supplementary Figure:

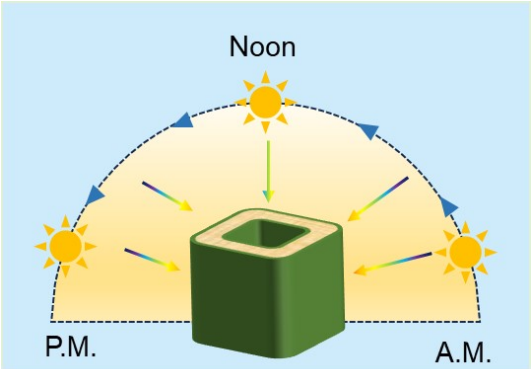

Figure S1. Schematic illustration of incident solar irradiance on each face of *Chimonobambusa quadrangularis*.

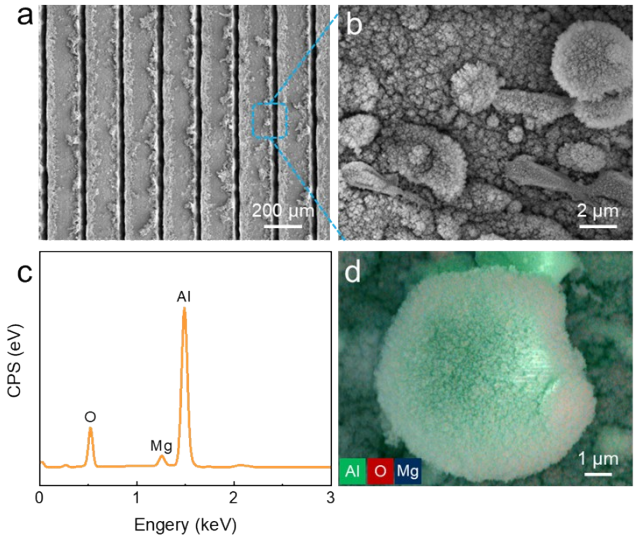

Figure S2 Characterization of the superhydrophilic microscale V-groove arrays (SMVAs). (a) Low- and (b) high-magnification SEM images of the V-groove structure. (c) Elemental mapping of aluminum, oxygen and magnesium. (d) Spatial distribution of aluminum, oxygen and magnesium on the microslot surface.

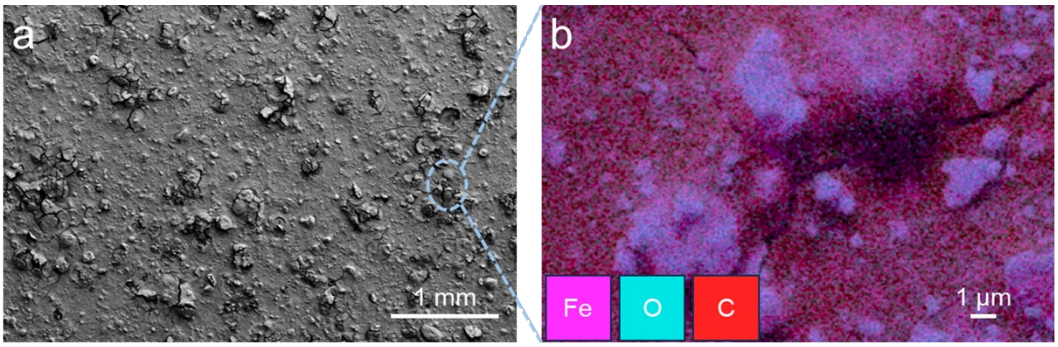

Figure S3. Surface morphology of the BC&Fe3O4 coating. (b) Elemental distribution of Fe, C and O elements on the surface.

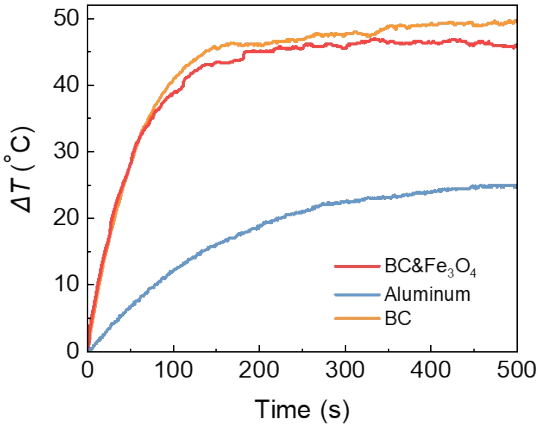

Figure S4. Time-dependent temperature variation of different photothermal coatings.

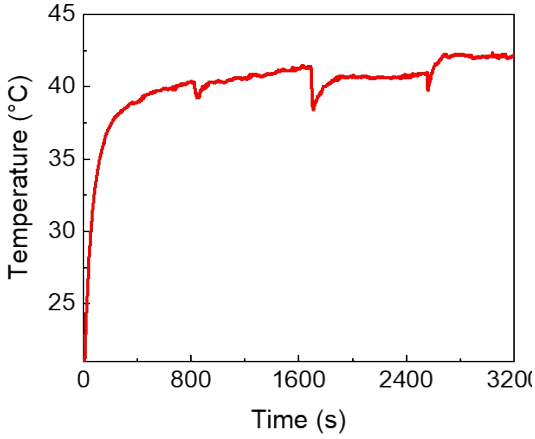

Figure S5. Temporal evolution of the average photothermal interface temperature under different illumination angles.

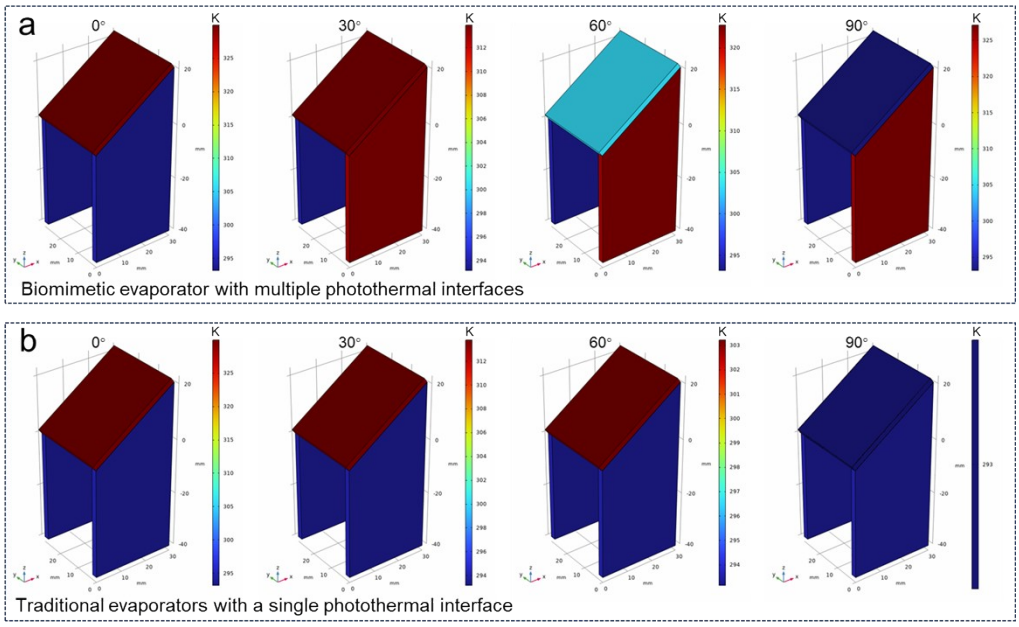

Figure S6 Simulated temperature rise of the photothermal interface for different evaporators using COMSOL Multiphysics 6.2: (a) biomimetic evaporator with multiple photothermal interfaces; (b) conventional evaporator with a single photothermal interface.

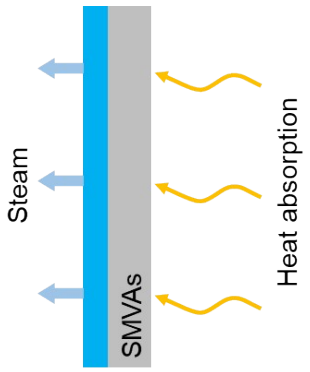

Figure S7. Schematic illustration of evaporation and heat absorption processes in SMVAs.

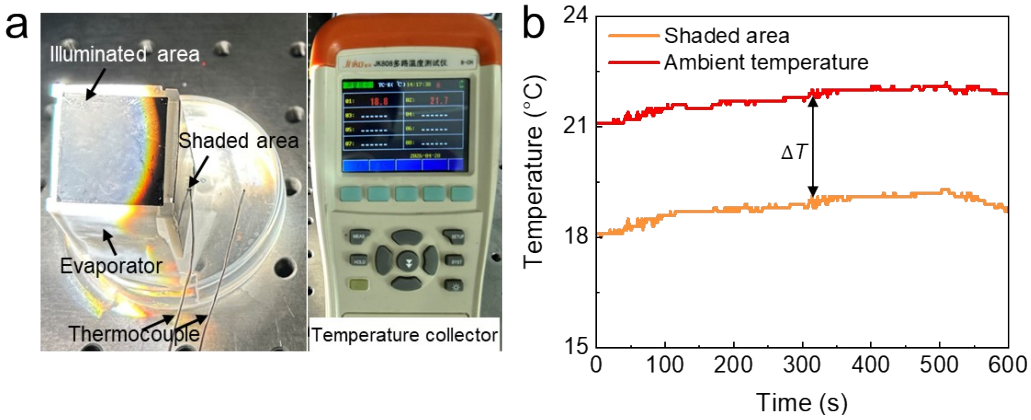

Figure S8 (a) (a) Photographs of the evaporator under illumination, with temperatures of the shaded region and the ambient environment indicated. (b) Time-dependent temperatures of the shaded region of the evaporator and the ambient environment.

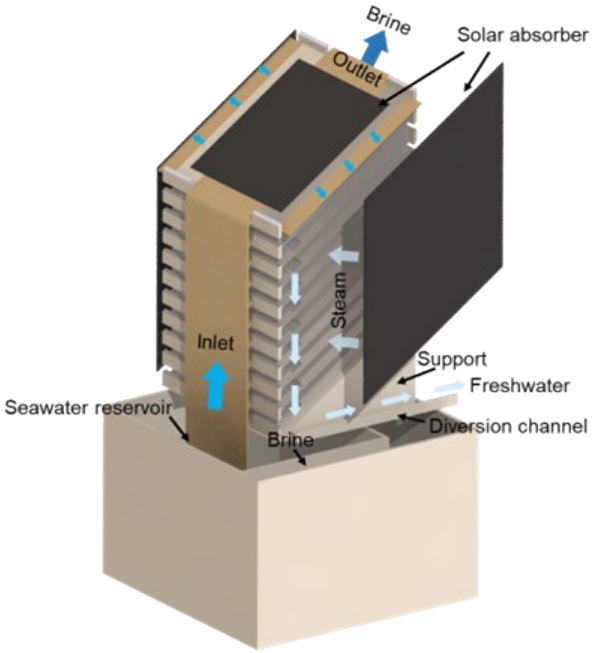

Figure S9. Schematic illustration of the multistage evaporator operating in seawater desalination mode.

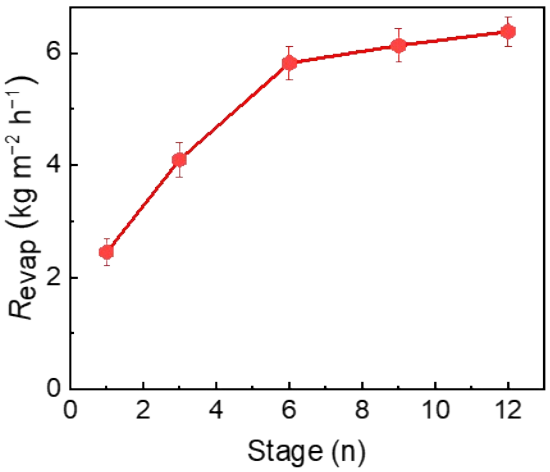

Fig. S10. Evaporation rates of the reverse multistage evaporator with different numbers of stages under one-sun illumination.

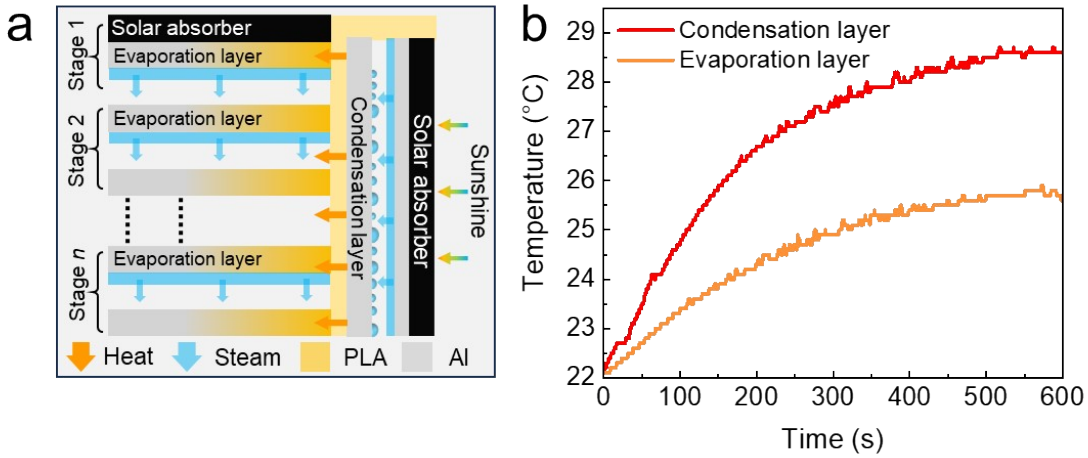

Figure S11 (a) Schematic illustration of the operating principle of an RME under horizontal illumination. (b) Time-dependent temperature rise of the side condensation layer and the intermediate evaporation layer.

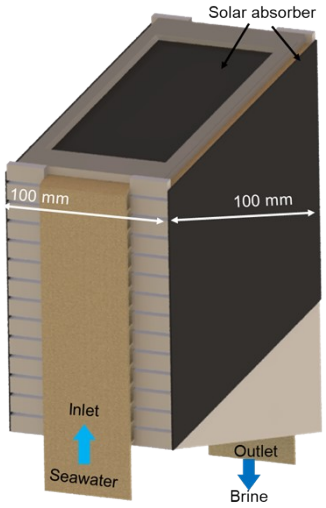

Figure S12 Schematic diagram of the RME (100 mm × 100 mm).

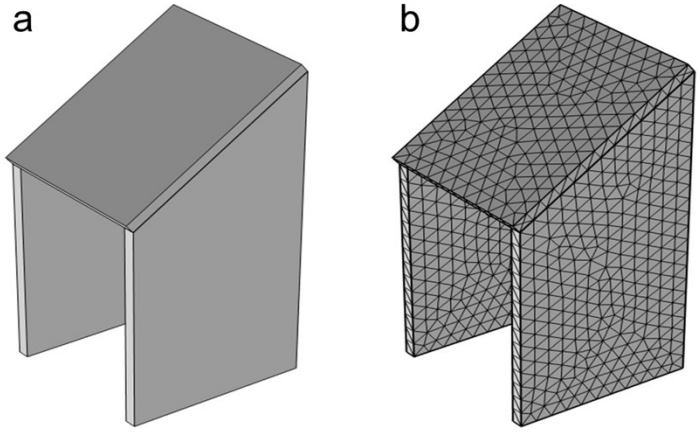

Fig. S13. Geometrical model of the bionic evaporator. (a) Three-dimensional model. (b) Partial mesh used in finite element simulations.